

Electron-nuclear decoupling at a spin clock transition

Krishnendu Kundu¹, Jia Chen^{2,3,4}, Silas Hoffman^{2,3,4✉}, Jonathan Marbey^{1,4,5}, Dorsa Komijani^{1,5}, Yan Duan⁶, Alejandro Gaita-Ariño⁶, John Stanton^{3,4,7}, Xiaoguang Zhang^{2,3,4}, Hai-Ping Cheng^{2,3,4✉} & Stephen Hill^{1,4,5✉}

The ability to design quantum systems that decouple from environmental noise sources is highly desirable for development of quantum technologies with optimal coherence. The chemical tunability of electronic states in magnetic molecules combined with advanced electron spin resonance techniques provides excellent opportunities to address this problem. Indeed, so-called clock transitions have been shown to protect molecular spin qubits from magnetic noise, giving rise to significantly enhanced coherence. Here we conduct a spectroscopic and computational investigation of this physics, focusing on the role of the nuclear bath. Away from the clock transition, linear coupling to the nuclear degrees of freedom causes a modulation and decay of electronic coherence, as quantified via electron spin echo signals generated experimentally and in silico. Meanwhile, the effective hyperfine interaction vanishes at the clock transition, resulting in electron-nuclear decoupling and an absence of quantum information leakage to the nuclear bath, providing opportunities to characterize other decoherence sources.

¹National High Magnetic Field Laboratory, Florida State University, Tallahassee, FL 32310, USA. ²Department of Physics, University of Florida, Gainesville, FL 32611, USA. ³Quantum Theory Project, University of Florida, Gainesville, FL 32611, USA. ⁴Center for Molecular Magnetic Quantum Materials, University of Florida, Gainesville, FL 32611, USA. ⁵Department of Physics, Florida State University, Tallahassee, FL 32306, USA. ⁶Instituto de Ciencia Molecular (ICMol), Universidad de Valencia, Paterna, Spain. ⁷Department of Chemistry, University of Florida, Gainesville, FL 32611, USA. ✉email: silas.hoffman@ufl.edu; hping@ufl.edu; shill@magnet.fsu.edu

The synthetic tunability of molecular nanomagnets provides a versatile platform for exploring and potentially harnessing their unique physical attributes for the development of next-generation quantum technologies^{1–4}. In particular, the electronic spin associated with a magnetic molecule may serve as the computational basis for a quantum bit, or qubit. However, as with any such system, protection from environmental noise that causes decoherence is of critical importance, representing one of the main hurdles on the path toward practical applications. In an attempt to suppress one of the more stubborn sources of decoherence arising from electron-nuclear interactions, various synthetic strategies have been employed such as nuclear spin patterning^{5,6} and the use of nuclear spin-free ligands^{7,8}. However, demonstration of long phase memory (coherence) times typically still requires extreme dilution in order to minimize electron spin–spin dephasing.

Rather than modifying the spin bath, an alternative approach involves exploiting so-called clock transitions⁹ at which the electron spin resonance (ESR) frequency is insensitive to the local magnetic induction and, therefore, does not couple to the fluctuating magnetic environment. Spin clock transitions occur at avoided level crossings associated with the Zeeman splitting of qubit basis states. This approach is well established in solid-state materials such as donor atoms in silicon^{10,11} or defect states in various other host crystals^{12–16}. Our interest is in molecular systems, for which enhanced coherence was demonstrated at a clock transition for a $[\text{Ho}(\text{W}_5\text{O}_{18})_2]^{9-}$ molecule by Shiddiq et al.¹⁷. Subsequently, clock transitions have been studied in other molecular systems^{18–22} and the effects of structural distortions have been analyzed theoretically for several Ho^{III} and V^{IV} complexes²³.

Here we directly investigate electron-nuclear coupling in the vicinity of a clock transition by means of pulsed electron spin-echo measurements and numerical modelling. Away from the clock transition, dipolar hyperfine coupling to the nuclear bath results in periodic modulations of the electronic coherence—the so-called electron spin-echo envelope modulation (ESEEM) effect²⁴. This modulation vanishes at the clock transition. Theoretically, we consider a minimal model that can host a clock transition: an $S=1$ spin subject to a relatively strong axial magnetic anisotropy, with an avoided Zeeman level crossing generated by a weaker transverse interaction (Fig. 1). We treat

coupling to the nuclear bath explicitly to reproduce the ESEEM effect via quantum dynamics simulations. The parameters in our simplified $S=1$ model are chosen to mimic the low energy physics of the $[\text{Ho}(\text{W}_5\text{O}_{18})_2]^{9-}$ molecule which, to the best of our knowledge, is the only system for which ESEEM has been characterized as a function of the applied magnetic field, \mathbf{B}_0 , in the vicinity of a clock transition. The simulations compare favorably with experiment, clearly demonstrating electron-nuclear decoupling at a spin clock transition. Although the experiments focus on $[\text{Ho}(\text{W}_5\text{O}_{18})_2]^{9-}$, our model applies quite generally for the coupling of an electronic spin to a finite nuclear bath. The combined study provides a microscopic view of the mechanism via which an electron spin qubit couples to nearby nuclei, in essence mediating leakage of quantum information to the nuclear bath.

Results

Electron spin resonance measurements. Pulsed ESR, which is central to most spin-based quantum device implementations²⁵, is an extremely powerful technique enabling both sample characterization and quantum control. The simplest illustration involves the two-pulse Hahn echo sequence^{24,26}, where a coherent superposition of spin “up” and “down” states is first generated via a $\pi/2$ rotation on the Bloch sphere, and then the magnetization is allowed to evolve freely in the xy -plane; this evolution is later inverted via application of a π -pulse, ideally refocusing any dephasing that occurs due to static disorder, resulting in the emission of an electron spin-echo at time 2τ after the initial $\pi/2$ pulse (τ is the delay between pulses). A dynamic environment causes decoherence²⁷, which manifests as a decay of the electron spin-echo intensity upon increasing τ . Meanwhile, coherent interactions with nearby quantum systems, e.g., other electrons or atomic nuclei, can give rise to a modulation of the electron spin-echo intensity²⁴. In particular, ESEEM arises due to the excitation of formally forbidden nuclear transitions during the pulsed electron spin-echo sequence, through hyperfine coupling to the central electron spin. Here, “central” refers to spins that have been prepared in a prescribed coherent quantum state, e.g., via the application of a $\pi/2$ pulse. ESEEM may therefore be used to characterize this aspect of the environment, providing extremely

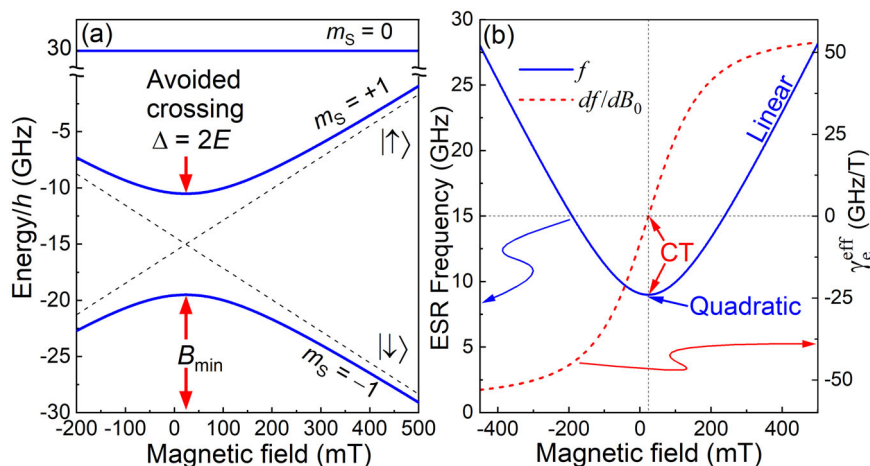


Fig. 1 Simulated HoW_{10} Zeeman diagram and ESR frequency. **a** Zeeman levels (solid blue lines) according to the Hamiltonian of Eq. (1), with the parameters given in the main text. An avoided crossing (a clock transition) between the two lowest-lying states (labeled $m_s = \pm 1$) is seen at $B_{\text{Oz}} = B_{\text{min}} = 23.6$ mT; the dashed lines denote the $m_s = \pm 1$ levels in the absence of an avoided crossing [i.e., E set to zero in Eq. (1)]. **b** ESR frequency, f (solid blue curve), corresponding to the transition between the $m_s = \pm 1$ states in **(a)**, and the associated effective gyromagnetic ratio, $\gamma_e^{\text{eff}} = df/dB_0$ (dashed red curve); the clock transition (CT) is indicated. Note that the ESR frequency couples linearly to B_0 far from the clock transition and quadratically at the clock transition, such that γ_e^{eff} crosses through zero.

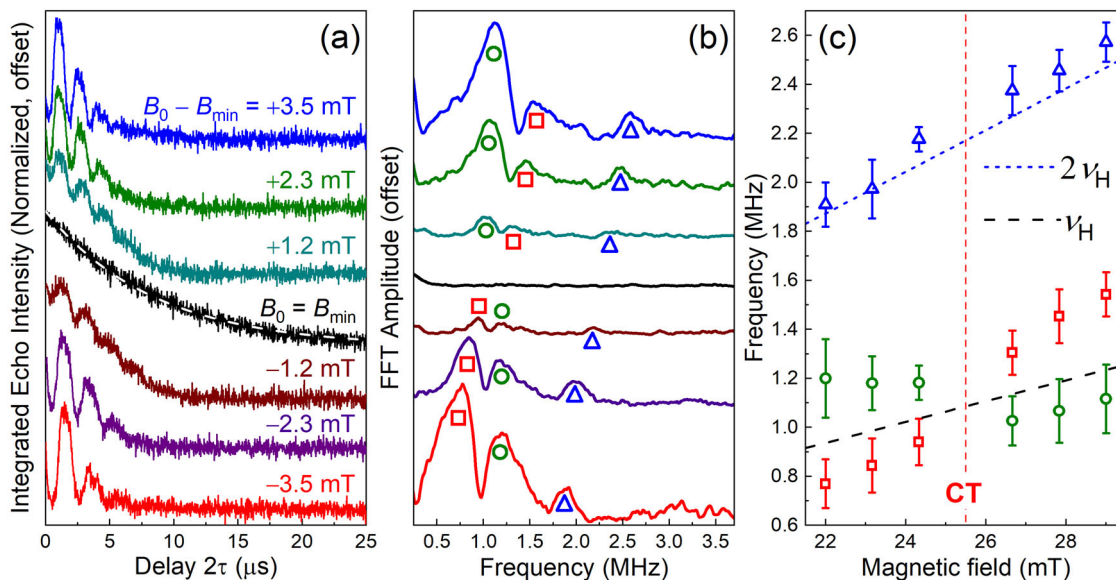


Fig. 2 Experimental HoW₁₀ ESEEM spectra. **a** Electron spin-echo decay curves recorded at 9.18 GHz and 5 K as a function of detuning, $B_0 - B_{\min}$ (see labeling); the white dash curve is fit to a mono-exponential decay for zero detuning ($B_0 = B_{\min}$), from which the optimum $T_m = 8.43(6) \mu\text{s}$ is deduced. **b** FFTs of the decay curves in (a), presented in the same order; prominent peaks in the ESEEM spectra are marked with red squares, green circles, and blue triangles. **c** Plot of the FFT peak frequencies in (b) versus B_0 , with error bars denoting \pm s.d. (approximating each peak as a Gaussian); the dashed lines correspond to harmonics of the proton Larmor frequency (see legend), the data points are color/shape coded according to the same scheme as those in (b), and the vertical dashed red line marks the clock transition (CT).

sensitive fingerprints of electron-nuclear decoherence mechanisms.

In order to gain microscopic insights into electron-nuclear coupling in the vicinity of a clock transition, ESEEM measurements were performed on a $\text{Na}_9[\text{Ho}_{0.001}\text{Y}_{0.999}(\text{W}_5\text{O}_{18})_2] \cdot n\text{H}_2\text{O}$ (hereon abbreviated HoW₁₀) single crystal, i.e., 0.1% HoW₁₀ doped into an isostructural non-magnetic YW₁₀ host crystal. Ho^{III} possesses a ground state spin-orbit coupled angular momentum, $J = L + S = 8$. The pseudo-axial coordination geometry imposed on the Ho^{III} ion results in a crystal field interaction that lifts the degeneracy of the $2J + 1$ projection (m_J) states, giving rise to a singlet and a series of $m_J \approx \pm i$ ($i = 1-8$) quasi-doublets, with the $m_J = \pm 4$ ground doublet lying $\approx 40 \text{ cm}^{-1}$ below the first excited crystal field states^{28,29}. A weak tetragonal crystal field interaction is effective in generating an avoided Zeeman level crossing between the $m_J = \pm 4$ basis states, thus giving rise to a 9.18 GHz clock transition^{17,30}. The hyperfine interaction involving the $I = \frac{7}{2}^{165}\text{Ho}$ nuclear spin further splits the $m_J = \pm 4$ states into $(2I + 1) = 8$ pairs of m_I sub-levels, resulting in eight avoided-crossings, i.e., eight clock transitions, four on either side of zero applied field¹⁷. We focus here on the lowest field clock transition (at $B_{0z} = 23.6 \text{ mT}$), which also gives the strongest ESEEM; note that, due to a small sample misalignment, this occurs at $B_0 = B_{\min} = 25.5 \text{ mT}$ in the present investigation (see the “Methods” section).

Electron spin-echo time traces recorded at a frequency of 9.18 GHz are shown in Fig. 2a for different detuning fields ($\Delta B = B_0 - B_{\min}$) from the clock transition, revealing strong temporal modulations (ESEEM) at most detunings. The first thing to note is the variation in decay time (\equiv phase memory time, T_m) and modulation depth as a function of the detuning. In particular, a complete absence of ESEEM and the maximum T_m is observed at zero detuning, i.e., at the clock transition. Fast Fourier transforms (FFT) of the time traces reveal three prominent peaks, highlighted by the red squares, green circles, and blue triangles in Fig. 2b. The associated ESEEM frequencies are plotted as a function B_0 in Fig. 2c; superimposed on the data are the 1st

and 2nd harmonics of the bare proton Larmor frequency, $\nu_H = \gamma_H B_0$, where $\gamma_H = 42.577 \text{ MHz/T}$ is the proton gyromagnetic ratio. The fact that the first two peaks (red squares and green circles) straddle the ν_H line and the third peak (blue triangles) lies on the $2\nu_H$ line is a strong indication that the ESEEM is caused by dipolar coupling to protons. This is not surprising given the significant amount of water in the lattice of $[\text{HoW}_{10}] \cdot n\text{H}_2\text{O}$ ($n \approx 35$ in fully solvated crystals). Indeed, a strong proton ESEEM effect is expected in this field range where the Ho–H dipolar coupling strength is comparable to the proton Larmor frequency (see below). By contrast, all other nuclei are predominantly non-magnetic, either due to low γ -values or a low abundance of magnetic isotopes.

A qualitative understanding of the ESEEM spectrum is obtained by first considering the simplest possible case of coupled $S = \frac{1}{2}$ and $I = \frac{1}{2}$ spins in the high-field limit in which $\nu_H > A$, where A ($= A_{zz}/h$, A_{zz} is the z -component of the hyperfine tensor) quantifies the bare dipolar coupling strength in frequency units. ESEEM arises due to the excitation of formally forbidden zero- and double-quantum transitions that rotate coupled electron and nuclear spins³¹. The modulation results from combinations of the allowed ($\nu_a = \gamma_e B_0 \pm \frac{1}{2} A$, γ_e is the electron gyromagnetic ratio) and formally forbidden ($\nu_f = \gamma_e B_0 \pm \nu_H$) transition frequencies at $|\nu_a^+ - \nu_f^-| = A$, $|\nu_f^+ - \nu_a^+| = |\nu_f^- - \nu_a^-| = \nu_H \pm \frac{1}{2} A$, and $|\nu_f^+ - \nu_f^-| = 2\nu_H$ ³¹. One may then understand the lowest two frequencies in Fig. 2c (red squares and green circles) as being due to the hyperfine coupled proton frequencies, $\nu_H \pm \frac{1}{2} A^{\text{eff}}$, where A^{eff} is an effective coupling strength on account of the physics that emerges at the clock transition (A^{eff} is further renormalized for HoW₁₀ due to the fact that $S \neq \frac{1}{2}$). Right at the clock transition, $A^{\text{eff}} \rightarrow 0$, which may be understood as being a consequence of the effective electron gyromagnetic ratio, γ_e^{eff} , crossing through zero at $B_0 = B_{\min}$ ($\gamma_e^{\text{eff}} \propto df/dB_0$ or $\langle \hat{S}_z \rangle$, the z -component spin expectation value); this is illustrated in Fig. 1b, where the ESR (clock) frequency couples quadratically to B_0 at the avoided crossing (clock transition), in contrast to the usual linear coupling

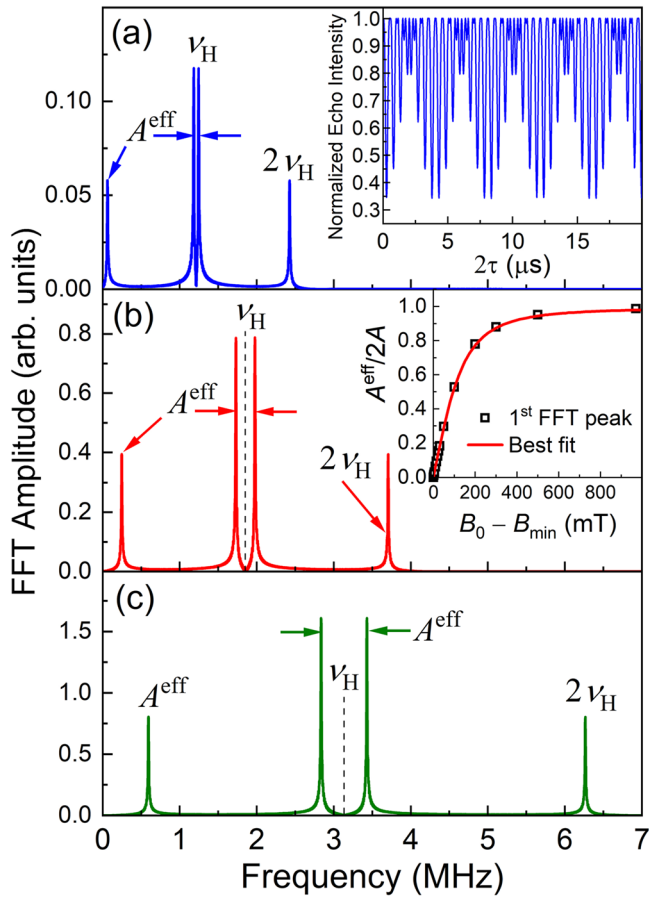


Fig. 3 Simulated ESEEM spectra for $N = 1$. FFTs of Hahn echo simulations for the simple case of a single $l = \frac{1}{2}$ proton coupled to a central $S = 1$ electron spin for different detunings, $B_0 - B_{\min} = +5$ mT (a), $+20$ mT (b), and $+50$ mT (c); see text for employed parameters. Several relevant frequencies are labeled in the FFT spectra. The inset in a shows a representative electron spin-echo intensity time trace. The inset in b plots A^{eff} deduced from the first FFT peak versus $B_0 - B_{\min}$ (error bars corresponding to \pm s.d. are considerably smaller than the data points and are not shown); the solid red curve is a simple fit that assumes $A^{\text{eff}} \propto df/dB_0$ from Fig. 1b.

far from the clock transition. This is why the ordering of red squares and green circles switches at the clock transition, i.e., there is a smooth evolution of $A^{\text{eff}} (\propto \gamma_e^{\text{eff}})$ such that it switches signs at the clock transition. This implies that the effective dipolar coupling to protons vanishes right at the clock transition; hence the ESEEM effect also vanishes at the clock transition, as does the electron-nuclear decoherence, leading to the steep rise in T_m observed upon approaching the clock transition [$= 8.43(6) \mu\text{s}$ at the clock transition]¹⁷. Meanwhile, the ESEEM modulation depth grows with the detuning, ΔB (i.e., with γ_e^{eff}), away from the clock transition, as does the electron-nuclear contribution to the central spin decoherence, i.e., T_m decreases to $\sim 1 \mu\text{s}$ far from the clock transition¹⁷.

The ESEEM effect is ultimately governed by the collective coupling of the Ho^{III} ion to the entire nuclear bath. However, the $1/r^3$ dependence of the dipolar interaction and large value of γ_H in comparison to other nuclei results in a spectrum that is dominated by nearby protons^{32,33}, the closest of which is $\sim 4 \text{ \AA}$ from the central Ho^{III} ion³⁰. At this separation and in the linear Zeeman regime [$\Delta B > 300$ mT, see Fig. 1b], the maximum Ho–H dipolar coupling strength, $A^{\text{max}} \approx 3 \text{ MHz}$ ($= 2\mu_0\mu_{\text{Ho}}\mu_{\text{H}}/4\pi hr^3$); this assumes $m_j = \pm 4$ for the ground state of Ho^{III}. The

experimental results displayed in Fig. 2 remain very far from this linear regime, which is why the separation of the red squares and green circles ($A^{\text{eff}} < 0.5 \text{ MHz}$) is well below the maximum. Meanwhile, ESEEM measurements far from the clock transitions are hampered by short phase memory times. Nevertheless, one would expect to observe strong ESEEM in proximity to most of the HoW₁₀ clock transitions due to the requirement that A^{eff} is of the same order as the proton Larmor frequency (see below), e.g., $\nu_H = 1.1 \text{ MHz}$ at 25.5 mT . Indeed, ESEEM is also observed at the 2nd ($\nu_H = 3.3 \text{ MHz}$) and 3rd ($\nu_H = 5.4 \text{ MHz}$) clock transitions (see Supplementary Discussion). Although the effect is less pronounced, the same qualitative behavior is found, i.e., a vanishing of the ESEEM at each clock transition and harmonic content centered at ν_H and $2\nu_H$. Therefore, the enhanced coherence in the vicinity of the clock transitions provides a window through which to observe ESEEM, which ultimately vanishes right at the clock transitions because $\gamma_e^{\text{eff}} \rightarrow 0$. We note that no modulation is discernible at the 4th clock transition ($\nu_H = 7.6 \text{ MHz}$), presumably because the effective dipolar coupling is just too weak in comparison to ν_H .

Numerical simulations. In order to gain microscopic understanding, we developed a simplified Hamiltonian for a central electron spin coupled to a finite proton spin bath. To preserve computational resources for the bath, we model the electronic system as an $S = 1$ spin with longitudinal and transverse anisotropy (Fig. 1a):

$$\hat{H}_S = D[\hat{S}_z^2 - \frac{1}{3}S(S+1)] + E(\hat{S}_x^2 - \hat{S}_y^2) + \gamma_e(B_0 - B_{\min})\hat{S}_z, \quad (1)$$

where the \hat{S}_j are spin-1 generators of rotation about axis j , while D and E are the second-order axial and rhombic zero-field splitting (anisotropy) parameters, respectively. B_{\min} is introduced to shift the clock transition away from $B_0 = 0$, mimicking the effect of the on-site hyperfine interaction with the ¹⁶⁵Ho nuclear spin; note that this field does not act on the proton bath. The eigenvectors of Eq. (1) at the clock transition (i.e., when $\Delta B = 0$) are $|\pm\rangle = \frac{1}{\sqrt{2}}(|\uparrow\rangle \pm |\downarrow\rangle)$ and $|0\rangle$, with energies $-\frac{1}{3}|D| \pm E$ and $+\frac{2}{3}|D|$, respectively. Here, $|\uparrow\rangle$, $|\downarrow\rangle$, and $|0\rangle$ are the states with $\langle \hat{S}_z \rangle = \pm 1$ and $\langle \hat{S}_x \rangle = 0$, respectively.

We set $D = -45 \text{ GHz}$, $|E| = 4.5 \text{ GHz}$ and $B_{\min} = 23.6 \text{ mT}$ in order to mimic the actual low-energy electronic structure of HoW₁₀. These parameters ensure the same clock transition frequency, $\Delta = 2E = 9 \text{ GHz}$, the same curvature of the two lowest lying levels, and a sizeable separation to the $|0\rangle$ state (Fig. 1). As an aside, because $|\pm\rangle$ are energetically well-separated from $|0\rangle$ in the vicinity of the clock transition, we can project onto the two-dimensional subspace defined by the former, wherein,

$$\begin{aligned} \hat{S}_z^2 &\rightarrow 1, \quad \hat{S}_z \rightarrow \sigma_x, \quad \hat{S}_x^2 - \hat{S}_y^2 \rightarrow \sigma_z, \quad \{\hat{S}_x, \hat{S}_y\} \rightarrow 2\sigma_y, \\ \hat{S}_x &\rightarrow 0, \quad \hat{S}_y \rightarrow 0, \quad \{\hat{S}_y, \hat{S}_z\} \rightarrow 0, \quad \{\hat{S}_z, \hat{S}_x\} \rightarrow 0. \end{aligned} \quad (2)$$

Using this notation, the Hamiltonian reduces to $\hat{H}_S \rightarrow E\sigma_z + \gamma\Delta B\sigma_x$, which precisely maps onto a ‘fictitious’ spin- $\frac{1}{2}$ model subjected to an effective magnetic field in the xz -plane³⁴. The eigenvectors, which are quantized along the effective field direction, are still denoted $|\pm\rangle$, although these are no longer equally weighted mixtures of $|\uparrow\rangle$ and $|\downarrow\rangle$ upon detuning from the clock transition. Nevertheless, at the clock transition ($\Delta B = 0$), one may visualize qubit operations within this subspace in terms of pure rotations around the j th axis of the Bloch sphere defined by $|\pm\rangle$, according to the Pauli matrices, σ_j ; the corresponding spin-1 operators are then easily found from Eq. (2). This mapping is helpful in understanding the simulated

Hahn-echo sequence (see the “Methods” section), as there is no simple analogy to the $S = \frac{1}{2}$ rotating frame for the actual $S = 1$ spin dynamics.

The nuclear spin bath, which ultimately causes decoherence and the observed ESEEM effect, is described by N protons coupled via dipolar interactions to the central $S = 1$ state

$$\hat{H}_{SI} = \hat{S}_z \sum_{m=1}^N \left[A_{sc}^m \hat{I}_z^m + A_{psc}^m (\hat{I}_x^m + \hat{I}_y^m) \right]. \quad (3)$$

Here, we employ secular (sc) and pseudosecular (psc) approximations with phenomenological couplings A_{sc}^m and A_{psc}^m , respectively; the \hat{I}_j^m are generators that rotate the spin of the m th proton around axis j . The pseudosecular interaction is often ignored due to averaging brought about by the mismatch in the proton Larmor and hyperfine frequencies. However, as previously discussed, this is not the case at the HoW₁₀ clock transitions. Indeed, the pseudosecular interaction turns out to be essential to the ESEEM effect because it is responsible for driving formally forbidden nuclear transitions during the Hahn echo sequence³¹. Meanwhile, the protons also undergo their own dynamics, independent of the central spin, according to

$$\hat{H}_I = - \sum_{m \neq n} D_{mn} (3 \cos^2 \theta_{mn} - 1) [2 \hat{I}_z^m \hat{I}_z^n - (\hat{I}_x^m \hat{I}_x^n + \hat{I}_y^m \hat{I}_y^n)] - \gamma_H B_0 \sum_{m=1}^N \hat{I}_z^m. \quad (4)$$

That is, each proton in the bath undergoes Larmor precession at a bare frequency $\gamma_H B_0$, and couples to other protons via a dipolar interaction of strength D_{mn} (~ 10 kHz); θ_{mn} is the angle between B_0 and the vector joining protons m and n . Energy-conserving proton flip-flop processes, driven by the $(\hat{I}_x^m \hat{I}_x^n + \hat{I}_y^m \hat{I}_y^n)$ term, are central to the electron spin decoherence process^{10,27,32,33}. To simulate the ESEEM, we numerically recreate the two-pulse Hahn echo sequence in silico by performing a time evolution according to the total Hamiltonian, $\hat{H}_{tot} = \hat{H}_S + \hat{H}_{SI} + \hat{H}_I$ (see the “Methods” section).

As a warm-up, we first consider the simple case of a single proton ($N = 1$) coupled to the central $S = 1$ spin, with $A = A_{sc} = 2A_{psc} = 1$ MHz. Figure 3a–c displays FFTs of the Hahn echo simulations for several detuning fields [inset to (a) displays a representative time trace]. In analogy to the $S = \frac{1}{2}$ case, we associate the lowest frequency FFT peak, and the splitting of the peaks on either side of ν_H , with the effective hyperfine interaction strength, A^{eff} ; the inset to Fig. 3b plots this frequency as a function of $B_0 - B_{\text{min}}$. As can clearly be seen, and in analogy with the experiments, $A^{\text{eff}} \rightarrow 0$ at the clock transition; consequently, the modulation depth is also zero at zero detuning. Meanwhile, far from the clock transition, such that $\gamma_e |B_0 - B_{\text{min}}| \gg |E|/h$, $A^{\text{eff}} \rightarrow 2A$; the factor of two is due to renormalization because $S = 1$ as opposed to $\frac{1}{2}$. Thus, in the high-field limit, FFT peaks occur at $2A$, $\nu_H \pm A$, and $2\nu_H$. Superimposed on the data in the inset to Fig. 3b is a phenomenological fit that assumes $A^{\text{eff}} \propto \gamma_e^{\text{eff}}$, deduced from df/dB_0 via Eq. (1). This confirms the idea that the variation in γ_e^{eff} (or $\langle \hat{S}_z \rangle$) in the vicinity of the clock transition governs the dipolar coupling of the central spin to the nearby proton. The final thing to note from the inset to Fig. 3a is the absence of decoherence, i.e., the peak electron spin-echo intensity does not decay. This is because the two-spin system executes perfectly coherent coupled dynamics, with no quantum phase leakage, i.e., there is no bath associated with this model.

In order to better capture the physics associated with the spin bath, we extend the model to $N = 7$ nuclear spins with a distribution of dipolar couplings to the central spin (Fig. 4a), enabling simulations of the ESEEM on reasonable timescales whilst also capturing the emergence of decoherence; we set

$(A_{sc}^m) = 2(A_{psc}^m) = 8$ MHz to best reproduce the experimental results (see the “Methods” section for further details). Time traces for several detunings on either side of the clock transition are displayed in Fig. 4b. As can be seen, the simulations qualitatively reproduce the experimental results in Fig. 2. A very clear ESEEM effect is observed with a modulation depth that increases with detuning, ΔB , while more-or-less vanishing right at the clock transition. The time traces also exhibit a very apparent decay in the coherence of the central spin dynamics, i.e., the finite spin bath model reproduces the experimentally observed decoherence of the central spin, including the maximum in T_m seen at the clock transition. Moreover, in spite of its simplicity, the simulated timescale associated with the decoherence is of the same order as the experiments. The only exception is at zero detuning, where the numerical decay is considerably flatter than the experiments. The residual decoherence observed at the clock transition in experiments is attributed to spin-lattice relaxation¹⁷, which is not included in our model; we comment on this further below. FFTs of the numerical time traces (Fig. 4c) are in excellent agreement with the experiment. Indeed, a plot of the center frequencies of the main FFT peaks as a function of detuning, $B_0 - B_{\text{min}}$ (Fig. 4d), reveals identical behavior to the experiments, i.e., a pair of peaks at $\nu_H \pm \frac{1}{2} A^{\text{eff}}$ and a higher frequency peak at $\sim 2\nu_H$. Once again, it can be seen that $A^{\text{eff}} \rightarrow 0$ at $B_0 = B_{\text{min}}$, and increases with detuning from the clock transition.

Discussion

The present experimental and theoretical investigation clearly demonstrates the effective decoupling of an electron spin qubit from the surrounding nuclear bath at a clock transition, going beyond previous studies that simply show evidence for enhanced coherence^{17,30}. In fact, the simulations reveal a pronounced enhancement in T_m at the clock transition, whereas the experiments on HoW₁₀ indicate that coherence is limited there by other factors. The primary culprit is spin-lattice (T_1) relaxation¹⁷. In particular, molecular vibrations that couple directly to the crystal field interaction(s) responsible for the clock transition (Fig. 1) may be expected to drive spin-lattice relaxation^{30,35,36}, an effect not included in our model. However, weak decoherence is observed even at the clock transition in the numerical simulations presented in Fig. 4. We attribute this to second-order coupling, $d^2 f/dB_0^2 = \gamma_e^2/\Delta$, i.e., df/dB_0 vanishes only precisely at the clock transition, and the HoW₁₀ qubit is therefore exposed to weak ¹H dipolar field fluctuations either side of B_{min} . This suggests that electron-nuclear decoupling should improve upon increasing the clock transition frequency since the second-order coupling scales inversely with Δ .

Electron spin–spin interactions have also been omitted from our model since we consider only one central Ho^{III} ion. One may expect the diagonal part of this interaction (i.e., $\hat{S}_z^m \hat{S}_z^n$) to decouple at a clock transition in exactly the same way that the proton bath decouples in this study, provided that the interaction is not too strong. As noted above, perfect decoupling occurs only to first-order ($df/dB_0 \rightarrow 0$) at the clock transition. However, second-order coupling should be weak if the spin–spin interaction strength is substantially weaker than the clock transition frequency ($\Delta = 2E$)^{10,22}, as is the case for well-separated (>nm) qubits. Meanwhile, although one may safely ignore angular momentum conserving electron–nuclear dipolar flip-flop processes in the present work because of the vastly different clock transition (Δ) and proton Larmor ($\gamma_H B_0$) frequency scales, this is not the case for electron spin–spin interactions. Dipolar coupling within arrays of nominally identical qubits will cause decoherence due to flip-flop processes between resonant electron spins ($\Delta_1 = \Delta_2$) via the $\hat{S}_x^m \hat{S}_x^n + \hat{S}_y^m \hat{S}_y^n$ interaction^{10,37}. Correctly modeling this physics

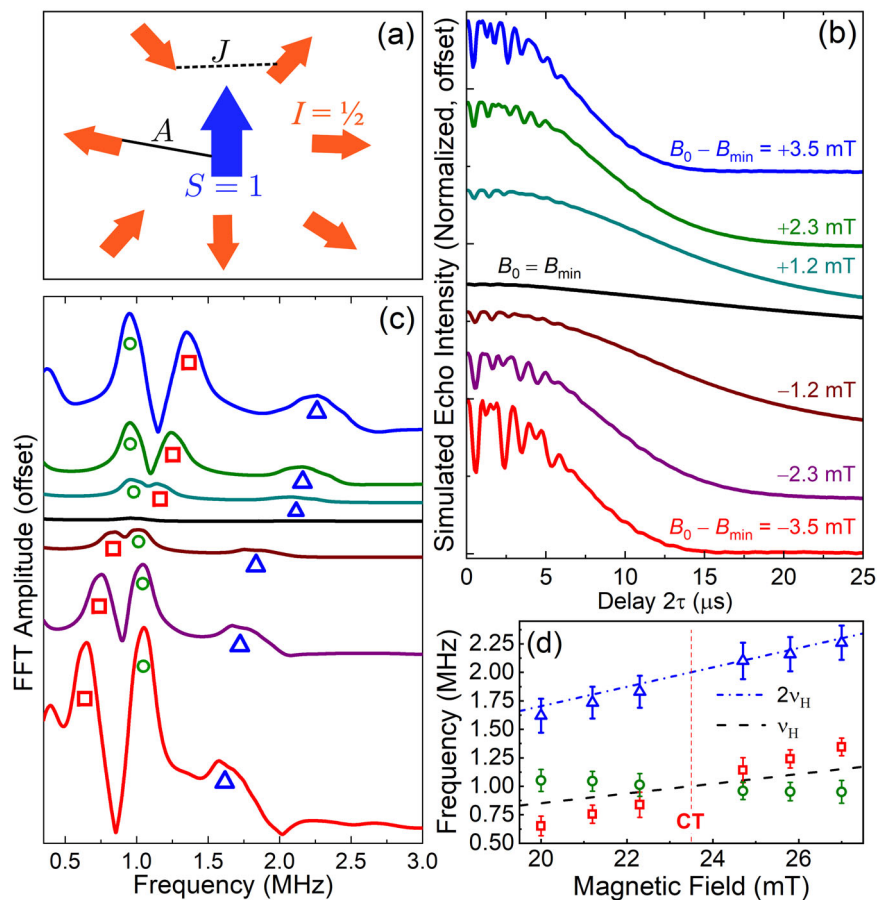


Fig. 4 Simulated ESEEM spectra for $N = 7$. **a** Schematic of the employed model consisting of a central $S = 1$ electron spin coupled to seven $I = \frac{1}{2}$ protons (see text for employed parameters). **b** Simulated ESEEM time traces as a function of the same detuning fields as Fig. 2 (see labeling). **c** FFTs of the time traces in (b), presented in the same order; prominent peaks are again marked with red squares, green circles, and blue triangles for direct comparison with Fig. 2. **d** Plot of the FFT peak frequencies in (c) as a function of B_0 , with error bars denoting \pm s.d. (approximating each peak as a Gaussian); the dashed lines correspond to harmonics of the proton Larmor frequency (see legend), the data points are color/shape coded according to the same scheme as those in (c), and the vertical dashed red line marks the clock transition (CT).

is more challenging, requiring a much larger bath with resonant and non-resonant qubits, due both to disorder (distributions in Δ) and a dynamic distribution of dipolar interactions within the ensemble. Such a model contains complex many-body physics that lies outside of the realm of the present investigation.

One may anticipate that future quantum devices based on molecular spins will feature controllable entangling interactions between individual qubits¹. Such control would enable the mitigation of resonant electron–electron spin flip-flop processes (or deliberate application of such two-qubit operations, when required). Likewise, quantum sensing applications involving single qubits are immune to this mode of decoherence. However, it is virtually impossible to remove all sources of magnetic noise, particularly nuclear spins, whilst maintaining the flexibility that molecular design principles allow. The present investigation, therefore, highlights the importance of clock transitions for suppressing electron–nuclear spin–spin decoherence. Moreover, one may expect these principles to apply quite generally to any type of clock transition. In this regard, hyperfine clock transitions show great promise due to weaker coupling to molecular vibrations²².

Methods

Experimental details. Since extensive discussions of sample preparation and handling, experimental setup and conditions, as well as the electronic properties that give rise to clock transitions in HoW₁₀ have been presented previously^{17,28},

only brief descriptions of essential details are given here. Single crystals of Na₉[Ho_{0.001}Y_{0.999}(W₅O₁₈)₂] \cdot *n*H₂O were prepared according to literature methods³⁸. ESEEM measurements were performed using a commercial Bruker E680 X-band spectrometer equipped with a cylindrical TE₀₁₁ dielectric resonator (model ER 4118 X-MD5, with an unloaded center frequency of 9.75 GHz), which was overcoupled to increase bandwidth and, thus, allow measurements at frequencies down to 9.1 GHz^{17,22}. The sample temperature was controlled using an Oxford Instruments CF935 helium flow cryostat and ITC503 temperature controller.

All of the data presented in this study (Fig. 2) were obtained for a single crystal. However, similar ESEEM behavior has been observed in experiments performed on many other crystals of varying Ho^{III} concentration¹⁷. Although in situ rotation of the crystal about a single-axis is possible, the low symmetry HoW₁₀ structure²⁸ and the need for rapid sample loading to avoid degradation due to solvent loss resulted in an $\sim 22.5^\circ$ misalignment between the applied field and the molecular magnetic easy- (*z*-) axis. This simply leads to a re-scaling of the clock transition fields: in this study, the lowest field clock transition occurs at $B_0 = B_{\min} = 25.5$ mT, which is equivalent to a longitudinal field, $B_{0z} = 23.6$ mT, where the *z*-direction defines the approximate HoW₁₀ four-fold symmetry axis. ESEEM results were derived from electron spin-echo decay curves generated using a standard two-pulse Hahn-echo sequence ($\pi/2 - \tau - \pi - \tau - \text{echo}$) as a function of detuning from the clock transition field, B_{\min} . The frequency domain plots in Fig. 2b were obtained by performing FFTs of the time traces, which were zero-padded by twice the number of data points and further smoothed using a 5-point average.

The spin Hamiltonian of the HoW₁₀ molecule may be described in terms of a set of axial crystal field parameters, B_k^q ($k = 2, 4, 6$, representing the rank of the associated crystal field operator, \hat{O}_k^q , and $q = 0$ the rotational order). Distortions away from the approximate D_{4d} point symmetry of the HoW₁₀ molecule engage the tetragonal crystal field interaction, $B_4^0 \hat{O}_4^0 \propto (\hat{S}_+^4 + \hat{S}_-^4)$ ²⁸, which is effective in generating avoided crossings between the eight hyperfine sub-level pairs associated with the $m_J = \pm 4$ ground doublet, resulting in clock transitions at magnetic fields,

$B_{\min} = \pm 23.6, \pm 70.9, \pm 118.1$ and ± 165.4 mT (for an applied field, B_0 , parallel to the molecular z -axis)¹⁷. The W and O nuclei in the HoW₁₀ molecular core are predominantly non-magnetic, with the exception of ¹⁷O ($I = \frac{5}{2}$, $\gamma = 5.77$ MHz/T) and ¹⁸³W ($I = \frac{1}{2}$, $\gamma = 1.77$ MHz/T) with 0.04% and 14.3% natural abundance, respectively. Moreover, their associated γ -values, along with those of the more distant ²³Na and ⁸⁹Y nuclei (both 100% abundance) are considerably smaller than those of the proton. Consequently, one would not expect to see strong ESEEM from coupling to these other nuclei, i.e., the assignment of the observed ESEEM to protons is unambiguous.

Theoretical details. The two-pulse Hahn echo sequence was recreated in silico by performing a time evolution according to the total Hamiltonian, $\hat{H}_{\text{tot}} = \hat{H}_S + \hat{H}_{\text{SI}} + \hat{H}_I$ ³³. The initial density matrix at thermal equilibrium was defined in the lab frame as

$$\rho_{\text{eq}} = \frac{\exp(-\beta \hat{H}_{\text{tot}})}{\text{Tr}(\exp(-\beta \hat{H}_{\text{tot}}))}, \quad (5)$$

where $\beta = h/k_B T$ and $T = 5$ K. Instantaneous $\pi/2$ and π pulses were performed according to the procedure described in the following paragraph. The density matrix was then allowed to evolve according to \hat{H}_{tot} for a time interval τ after each pulse. Finally, the echo intensity was evaluated by computing the expectation value of the z -component of the Ho^{III} magnetization in the lab frame, $\text{Tr}_I(\rho \hat{S}_z)$, with the trace taken over the nuclear states. Exact matrix diagonalization demands considerable computational resources. Therefore, in order to carry out these calculations on reasonable time scales, a number of compromises were necessary. Foremost among these was the limitation on the size of the nuclear spin bath to $N = 7$ protons. Meanwhile, based on a priori knowledge of the spin dynamics, we could also optimize the time step and duration of the simulations, i.e., the time step (100 ns) results in a frequency cut-off, which we set to well above the $2\nu_H$ frequency seen in the experimental spectra (Fig. 2), and the duration (100 μ s) was chosen to ensure an FFT resolution comparable to the experiments.

As discussed in the main text, the low energy $|\pm\rangle$ eigenvectors at the clock transition are not the usual $|\uparrow\rangle$ and $|\downarrow\rangle$ states relevant to the $S = \frac{1}{2}$ case; indeed, there is no simple rotating frame analogy that can easily be visualized in the case of the 'real' $S = 1$ system. One must therefore take care applying appropriate $\pi/2$ and π pulses in order to generate the echo. In fact, one may reduce the problem to the simple Bloch sphere picture via projection onto the two-dimensional $|\pm\rangle$ subspace according to Eq. (2), i.e., a 'fictitious' spin- $\frac{1}{2}$ subjected to an effective magnetic field in the xz -plane ($\hat{H}_S \rightarrow E\sigma_z + \gamma_e \Delta B \sigma_x$)³⁴. The appropriate pulses can then be implemented via rotations about any axis that is perpendicular to the effective field, $\vec{B}^{\text{eff}} (= \sqrt{E^2 + (\gamma_e \Delta B)^2})$. Exactly at the clock transition ($\Delta B = 0$), where $\vec{B}^{\text{eff}} \parallel z$, this is easily achieved using either the pure σ_x or σ_y Pauli matrix, corresponding to the spin-1 operators \hat{S}_z and $\{\hat{S}_x, \hat{S}_y\}$, respectively. Away from the clock transition, \vec{B}^{eff} tilts towards x within the $|\pm\rangle$ subspace. We, therefore, employ a pure σ_y rotation, which does not depend on the orientation of \vec{B}^{eff} , i.e., we implement pulses of the form $\exp[i\phi(\hat{S}_x, \hat{S}_y)/2]$, where ϕ denotes the rotation angle in radians. Although the $\{\hat{S}_x, \hat{S}_y\}$ operator has no direct correspondence with the microwave B_1 field employed in the experiments, it conveniently achieves the desired result. Moreover, it is formally equivalent to operating with \hat{S}_z at the clock transition, which does correspond directly to the experimental parallel mode B_1 field. However, upon moving away from the clock transition, the ideal magnetic \hat{S}_z -pulse evolves with the applied field, B_0 , as the eigenvectors acquire unequal $|\uparrow\rangle$ and $|\downarrow\rangle$ weights. Indeed, the durations of the $\pi/2$ and π pulses employed in the real experiments had to be optimized for each field step, something that could be avoided in the simulations by implementing pure σ_y rotations.

Additional subtleties of the calculations concern the precise details of the microscopic interactions. For example, in order to recreate a realistic proton bath, a distribution of electron-nuclear hyperfine coupling strengths, $A^m = A_{\text{sc}}^m = 2A_{\text{psc}}^m$ ($m = 1$ to N), was generated with random values in the range from 7 to 9 MHz such that $\langle A \rangle = 8$ MHz. Likewise, the distribution of proton-proton dipolar interactions was implemented by fixing the coupling strength in Eq. (4), $D_{mn} = \mu_{\text{H}}^2 / 8\pi r^3 \approx 10$ kHz (≈ 1.8 Å distance), and randomizing the angle θ_{mn} . To compensate for the small size of the nuclear bath, the simulations were repeated 10 times for different A^m and θ_{mn} randomizations, then averaged; this approach is obviously vastly more efficient computationally compared to increasing the bath size by a factor of ten. Not only do these measures better mimic the real [HoW₁₀]· n H₂O system, they avoid the highly unphysical situation in which the seven protons are indistinguishable, with identical couplings to the central spin and to each other. The 8 MHz value for $\langle A \rangle$ was chosen so as to reproduce the effective hyperfine interaction seen in the experiments, i.e., the frequency splittings between the red squares and green circles in Figs. 2c and 4d. This corresponds to a Ho-¹H separation of ~ 2.9 Å, which is a little below the known closest distance (~ 4 Å), which we attribute to the fact that the model under-counts the number of nearby protons by about an order of magnitude, i.e., $n = 35$ H₂O molecules, or 70 protons per Ho^{III} ion. Consequently, the smaller distance employed in the simulations

effectively renormalizes the collective hyperfine coupling strength. Finally, the frequency-domain plots in Fig. 4c and d were obtained by first subtracting a stretched exponential background from the time traces (Fig. 4b), then performing FFTs of the residual ESEEM modulations; Fourier-transform filtering was then used to smooth the resulting frequency-domain plots.

In spite of the aforementioned simplifying assumptions, the employed model captures the essential physics associated with the ESEEM effect in the vicinity of a realistic clock transition. Moreover, the simulations reproduce the experimentally observed electron-nuclear decoherence. Approximate cluster correlation expansion (CCE) methods are able to consider a much larger and more realistic bath consisting of thousands of protons. Indeed, such studies applied to simple spin- $\frac{1}{2}$ qubits (with no clock transition) obtain essentially perfect quantitative agreement with experimental phase memory times³². However, they also reveal that decoherence is dominated by stochastic flip-flop processes associated with proton pairs that are relatively close (a few Å) to the central electron spin. As such, the exact quantum calculations considered here contain the same ingredients. It is therefore unsurprising that the obtained phase memory times agree with the experiment to within approximately a factor of two. Indeed, the $N = 7$ model enables the exploration of many other microscopic aspects of the bath that influence decoherence. We hope to explore this further in the future. We wish to emphasize, however, that it was not our original intent to quantitatively reproduce the decoherence, but rather to qualitatively reproduce the ESEEM effect in the vicinity of a clock transition, something that this investigation has achieved.

Data availability

Supplementary Information (experimental HoW₁₀ ESEEM data at the 2nd and 3rd clock transitions) is linked to the online version of this article. All data that support the findings of this study are available via the Open Science Framework (OSF: <https://osf.io/EQMWN>) with the identifier <https://doi.org/10.17605/OSF.IO/EQMWN>.³⁹ This includes all of the data files generated from the experiments and numerical simulations presented in Figs. 1–4, as well as Figs. S1 and S2 presented in the Supplementary Information.

Code availability

The computer code used for the numerical simulations is available via the GitHub repository.⁴⁰

Received: 28 September 2021; Accepted: 10 February 2023;

Published online: 27 February 2023

References

- Gaita-Ariño, A., Luis, F., Hill, S. & Coronado, E. Molecular spins for quantum computation. *Nat. Chem.* **11**, 301–309 (2019).
- Atzori, M. & Sessoli, R. The second quantum revolution: role and challenges of molecular chemistry. *J. Am. Chem. Soc.* **141**, 11339–11352 (2019).
- Godfrin, C. et al. Operating quantum states in single magnetic molecules: implementation of Grover's quantum algorithm. *Phys. Rev. Lett.* **119**, 187702 (2017).
- Bayliss, S. L. et al. Optically addressable molecular spins for quantum information processing. *Science* **370**, 1309–1312 (2020).
- Graham, M. J., Yu, C.-J., Krzyaniak, M. D., Wasielewski, M. R. & Freedman, D. E. Synthetic approach to determine the effect of nuclear spin distance on electronic spin decoherence. *J. Am. Chem. Soc.* **139**, 3196–3201 (2017).
- Jackson, C. E., Lin, C.-Y., Johnson, S. H., van Tol, J. & Zadrozny, J. M. Nuclear-spin-pattern control of electron-spin dynamics in a series of V(IV) complexes. *Chem. Sci.* **10**, 8447–8454 (2019).
- Zadrozny, J. M., Niklas, J., Poluektov, O. G. & Freedman, D. E. Millisecond coherence time in a tunable molecular electronic spin qubit. *ACS Cent. Sci.* **1**, 488–492 (2015).
- Yu, C.-J. et al. Long coherence times in nuclear spin-free vanadyl qubits. *J. Am. Chem. Soc.* **138**, 14678–14685 (2016).
- Bollinger, J. J., Prestage, J. D., Itano, W. M. & Wineland, D. J. Laser-cooled-atomic frequency standard. *Phys. Rev. Lett.* **54**, 1000–1003 (1985).
- Wolfowicz, G. et al. Atomic clock transitions in silicon-based spin qubits. *Nat. Nanotechnol.* **8**, 561–564 (2013).
- Morello, A., Pla, J. J., Bertet, P. & Jamieson, D. N. Donor spins in silicon for quantum technologies. *Adv. Quantum Technol.* **3**, 2000005 (2020).
- Stark, A. et al. Clock transition by continuous dynamical decoupling of a three-level system. *Sci. Rep.* **8**, 1–8 (2018).
- Miao, K. C. et al. Universal coherence protection in a solid-state spin qubit. *Science* **369**, 1493–1497 (2020).
- Hemmer, P. Multiplicative suppression of decoherence. *Science* **369**, 1432–1433 (2020).

15. Probst, S. et al. Hyperfine spectroscopy in a quantum-limited spectrometer. *Magn. Reson.* **1**, 315–330 (2020).
16. Onizhuk, M. et al. Probing the coherence of solid-state qubits at avoided crossings. *PRX Quantum* **2**, 010311 (2021).
17. Shiddiq, M. et al. Enhancing coherence in molecular spin qubits via atomic clock transitions. *Nature* **531**, 348–351 (2016).
18. Harding, R. T. et al. Spin resonance clock transition of the endohedral fullerene $^{15}\text{N}@C_{60}$. *Phys. Rev. Lett.* **119**, 140801 (2017).
19. Zadrozny, J. M., Gallagher, A. T., Harris, T. D. & Freedman, D. E. A porous array of clock qubits. *J. Am. Chem. Soc.* **139**, 7089–7094 (2017).
20. Collett, C. A. et al. A clock transition in the Cr₇Mn molecular nanomagnet. *Magnetochemistry* **5**, 4 (2019).
21. Collett, C. A., Santini, P., Carretta, S. & Friedman, J. R. Constructing clock-transition-based two-qubit gates from dimers of molecular nanomagnets. *Phys. Rev. Res.* **2**, 032037 (2020).
22. Kundu, K. et al. 9.2 GHz clock transition in a Lu(II) molecular spin qubit arising from a 3467 MHz hyperfine interaction. *Nat. Chem.* **14**, 392–397 (2020).
23. Giménez-Santamarina, S., Cardona-Serra, S., Clemente-Juan, J. M., Gaita-Ariño, A. & Coronado, E. Exploiting clock transitions for the chemical design of resilient molecular spin qubits. *Chem. Sci.* **11**, 10718–10728 (2020).
24. Schweiger, A. & Jeschke, G. *Principles of Pulse Electron Paramagnetic Resonance* (Oxford University Press on Demand, 2001).
25. Wolfowicz, G. & Morton, J. J. L. Pulse techniques for quantum information processing. *eMagRes* **5**, 1515–1528 (2016).
26. Hahn, E. L. Spin echoes. *Phys. Rev.* **80**, 580–594 (1950).
27. Prokofev, N. V. & Stamp, P. C. E. Theory of the spin bath. *Rep. Prog. Phys.* **63**, 669–726 (2000).
28. Ghosh, S. et al. Multi-frequency EPR studies of a mononuclear holmium single-molecule magnet based on the polyoxometalate $[\text{Ho}(\text{W}_5\text{O}_{18})_2]^{9-}$. *Dalton Trans.* **41**, 13697–13704 (2012).
29. Vonci, M. et al. Magnetic excitations in polyoxotungstate-supported lanthanoid single-molecule magnets: an inelastic neutron scattering and ab initio study. *Inorg. Chem.* **56**, 378–394 (2017).
30. Liu, J. et al. Quantum coherent spin-electric control in a molecular nanomagnet at clock transitions. *Nat. Phys.* **17**, 1205–1209 (2021).
31. Goldfarb, D. & Stoll, S. (eds) *EPR Spectroscopy: Fundamentals and Methods (eMagRes)* (John Wiley and Sons, 2018).
32. Canarie, E. R. & Stoll, S. Quantitative structure-based prediction of electron spin decoherence in organic radicals. *J. Phys. Chem. Lett.* **11**, 3396–3400 (2020).
33. Chen, J. et al. Decoherence in molecular electron spin qubits: insights from quantum many-body simulations. *J. Phys. Chem. Lett.* **11**, 2074–2078 (2020).
34. Vega, S. & Pines, A. Operator formalism for double quantum NMR. *J. Chem. Phys.* **66**, 5624–5644 (1977).
35. Kragoskow, J. G. C. et al. Analysis of vibronic coupling in a 4f molecular magnet with FIRMS. *Nat. Commun.* **13**, 825 (2022).
36. Ullah, A. et al. Electrical two-qubit gates within a pair of clock-qubit magnetic molecules. *npj Quantum Inf.* **8**, 133 (2022).
37. Escalera-Moreno, L., Gaita-Ariño, A. & Coronado, E. Decoherence from dipolar interspin interactions in molecular spin qubits. *Phys. Rev. B* **100**, 064405 (2019).
38. AlDamen, M. A. et al. Mononuclear lanthanide single molecule magnets based on the polyoxometalates $[\text{Ln}(\text{W}_5\text{O}_{18})_2]^{9-}$ and $[\text{Ln}(\beta_2\text{-SiW}_{11}\text{O}_{39})_2]^{13-}$ (Ln^{III} = Tb, Dy, Ho, Er, Tm, and Yb). *Inorg. Chem.* **48**, 3467–3479 (2009).
39. Hill, S. et al. *Electron-Nuclear Decoupling at a Spin Clock Transition*. OSF. <https://osf.io/EQMWN> (2023).
40. Kundu, K. *ESEEM*. GitHub. <https://github.com/krishmaglab/ESEEM> (2023).

Acknowledgements

We are grateful to Eugenio Coronado and Shimon Vega for the insightful discussion, and we thank Haechan Park and James Fry for assistance in estimating the closest Ho–¹H distances. The spectroscopic and theoretical work reported in this paper was supported by the Center for Molecular Magnetic Quantum Materials (M²QM), an Energy Frontier Research Center funded by the US Department of Energy, Office of Science, Basic Energy Sciences under Award DE-SC0019330. Experimental work performed at the National High Magnetic Field Laboratory is supported in part by the National Science Foundation (under DMR-1644779 and DMR-2128556) and the State of Florida. Synthesis of the HoW₁₀ sample was supported by: the EU (ERC-2018-AdG-788222 MOL-2D, the QUANTERA project SUMO, and FET-OPEN grant 862893 FATMOLS); the Spanish MCIU (grant CTQ2017-89993 and PGC2018-099568-B-I00 co-financed by FEDER, grant MAT2017-89528; the Unit of excellence ‘Mariade Maeztu’ CEX2019-000919-M); and the Generalitat Valenciana (Prometeo Program of Excellence).

Author contributions

Y.D. prepared the HoW₁₀ sample. The experiments were conceived and designed by S. Hill and D.K., while D.K. performed the measurements. D.K., J.M., and S. Hill analyzed the experimental results. S. Hoffman developed the theory. K.K. and J.C. performed the simulations. The manuscript was written by J.C., J.M., and S. Hill with contributions from S. Hoffman, K.K., A.G., and X.Z. J.S., A.G., X.Z., H.-P.C., and S. Hill supervised the research.

Competing interests

The authors declare no competing interests.

Additional information

Supplementary information The online version contains supplementary material available at <https://doi.org/10.1038/s42005-023-01152-w>.

Correspondence and requests for materials should be addressed to Silas Hoffman, Hai-Ping Cheng or Stephen Hill.

Peer review information *Communications Physics* thanks Junjie Liu and the other, anonymous, reviewers for their contribution to the peer review of this work.

Reprints and permission information is available at <http://www.nature.com/reprints>

Publisher’s note Springer Nature remains neutral with regard to jurisdictional claims in published maps and institutional affiliations.



Open Access This article is licensed under a Creative Commons

Attribution 4.0 International License, which permits use, sharing, adaptation, distribution and reproduction in any medium or format, as long as you give appropriate credit to the original author(s) and the source, provide a link to the Creative Commons license, and indicate if changes were made. The images or other third party material in this article are included in the article’s Creative Commons license, unless indicated otherwise in a credit line to the material. If material is not included in the article’s Creative Commons license and your intended use is not permitted by statutory regulation or exceeds the permitted use, you will need to obtain permission directly from the copyright holder. To view a copy of this license, visit <http://creativecommons.org/licenses/by/4.0/>.

© The Author(s) 2023